

A Synergistic Combination of AuNRs and C Dots as a Multifunctional Material for Ice Recrystallization Inhibition and Rapid Rewarming

Shenyi Ding, Sarmad Ali,* Shudong Zhang, Jun Zhao, Cui Liu, Muhammad Adnan Aslam, Xinling Yu, Min Xi,* Lei Pan, Nian Li,* and Zhenyang Wang



Cite This: *ACS Omega* 2023, 8, 10466–10475



Read Online

ACCESS |



Metrics & More

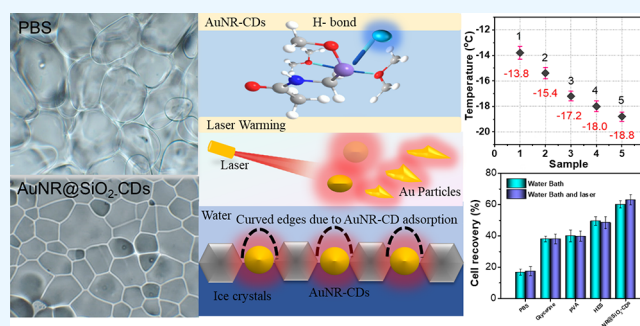


Article Recommendations



Supporting Information

ABSTRACT: Robust platforms and advanced biocompatible materials having diverse performances are in tremendous demand for cryopreservation of biocells, which are greatly limited by the crystallization, formation, and growth of ice crystals. The fickle structure and the arduous extraction process of modern attainable antifreezing proteins cause fatal cryoinjury of the cells making it challenging to develop anti-icing materials. Thus, designing Au colloids is an effective way to combat cell-damaging concerns during the ice freezing–thawing process. Herein, we propose an emerging biomimetic hybrid nanomaterial (AuNR@SiO₂-CDs) prepared by combining the photoheating and rewarming controlling characteristics of carbon dots (CDs) and gold nanorods (AuNRs), respectively, via a SiO₂ scaffold that has an optimal aspect ratio of ~4.4. The performance of the material is applied in the freezing and resuscitation of HeLa cells. The typical linkage between the AuNR and CDs not only retains the stable structure but also possesses the symmetric functional characteristics of affirmative cryoprotectant materials and sustained low cytotoxicity of cell viability >90%. The cell recovery rate of the HeLa cell is significantly improved to ~60%, which is propped up to >4% higher by the laser irradiation dose. The above hybrid material is paving a path toward novel bionic antifreezing proteins and is envisioned for ice recrystallization inhibition and rapid rewarming.



1. INTRODUCTION

In the course of freezing and thawing or rewarming, controlling the ice crystals' formation, growth, and then recrystallization influences all aspects of human activities.^{1–5} From transportation, cryopreservation, and industrial production to biomedical and other fields, ice is directly or indirectly involved, which is somehow lethal to living things at the macro/micro level.⁶ Intensive investigations have been carried out to control and inhibit ice growth and recrystallization including unique approaches by nature, but materials with favorable ice inhibition characteristics are still insufficient.

For instance, natural antifreeze materials (AFPs) can prevent ice growth and recrystallization at low temperatures via three tuning effects, namely, dynamic ice shaping (DIS), thermal retardation (TH), and ice recrystallization inhibition (IRI). However, the application scope of AFPs is inherently limited by their high extraction cost, easy inactivation, and high cytotoxicity.^{6,7} Therefore, recently, some other synthetic inhibitors with the same ice regulation ability as that of AFPs such as biopolymers and hydrogels,^{8,9} graphene oxide (GO),¹⁰ and a variety of carbon dots (CDs) have been devoted as novel materials for cryopreservation applications, among which CDs^{11,12} are considered as a new kind of hot material at present due to their advantages of small size, low

biotoxicity, and convenient preparations. Moreover, oxygen-containing groups and the existence of a carbon–carbon single bond make it easy to combine with ice crystals.^{13–15} Parvin and others¹⁶ discovered that fluorescent substances are excreted from the body, verifying that CDs have good biocompatibility for organisms or cells. Bai et al.¹¹ reported nitrogen-doped CDs (OQCN) for cryopreservation where OQCN produces the Kelvin effect through a hydrogen bond to inhibit the ice growth of red blood cells. Ice crystals mainly have to carry mechanical damage and inactivation of biocells during the cryopreservation, freezing, and rewarming process.¹⁷ Therefore, it is necessary to effectively regulate the evolution of ice crystals to improve the cell survival rate. Recently, Wang et al.¹² via glucose as a precursor studied the hydrothermal synthesis of the glucose-carbon point (G-CD), which exhibits a high IRI ability and was able to enhance the

Received: January 5, 2023

Accepted: February 28, 2023

Published: March 8, 2023



recovery rate of sheep red blood cells from freezing and rewarming to 60%.

During the rewarming process, the slower rate of warming can lead to the nucleation and growth of ice. Even under the action of cryoprotectants, if the temperature does not rise above the melting point of water in time, the ice crystals will inevitably recrystallize and cause damage to the cells. In short, cryopreservation requires the optimal cooling and rewarming conditions to locate and combat ice formation and cell injury.¹⁷ A number of nanomaterials have been used for reheating ice such as magnetic nanoparticles, graphene oxide (GO),¹⁰ molybdenum disulfide (MoS₂),¹⁸ and gold nanorods (AuNRs).¹⁹ Ketterer²⁰ found that the rewarmed kidney samples via a microwave oven provided bulky ice crystals due to uneven heating, which are unsuitable for cell cryopreservation. Consequently, other techniques such as electric, vibrational, and electromagnetic heating are practiced to water and are able to change the aggregation state of water molecules, elevate the icing energy barrier, and accelerate the temperature. Unfortunately, the above techniques cause damage to cell biology.^{7,21} Recently, a promising methodology called laser-assisted reheating is considered to be a more effective rewarming method than traditional water baths. Interestingly, some of the nanomaterials have the ability to convert laser energy into heat energy to improve heating efficiency, reduce cell damage during cryopreservation, and improve cell survival, among which gold nanorods have the most excellent photothermal effect, which can quickly heat up under laser irradiation, avoiding secondary damage to cells caused by ice crystals during the rewarming process.^{18,22} Also, the gold nanorods' aspect ratio is generally in between 2 and 25, resembling one-dimensional nanoparticles. Anisotropic optical properties like local surface plasmon resonance (LSPR), surface-enhanced Raman scattering, and photothermal conversion due to their versatile morphology are of great application value in optical sensing, biological imaging, detection, diagnosis, and treatment.^{23–25}

In the present work, inspired by the antifreeze properties of AFPs, biomimetic antifreeze nanomaterials with similar characteristics have been prepared. We utilize the individual properties of both CDs and gold nanorods to combine with a certain aspect ratio of ~4.4 through silicon oxide binders. The combination holds a new biomimetic antifreeze material characteristic. Furthermore, its performance in ice recrystallization inhibition and its application to cell cryopreservation and rapid rewarming were explored. We found that the synthesized hybrid material (AuNR@SiO₂-CDs) could reduce ice growth and recrystallization. The cryopreservation and rewarming of HeLa cells elaborated that the materials also have a better cell recovery performance rate than other common cryoprotectants. The icing temperature decreased down to 5 °C, and the recovery of cells after rewarming under 808 nm laser irradiation was significantly improved as well. To the best of our knowledge, this perspective of the AuNR-CD combination is not reported elsewhere.

2. EXPERIMENTAL SECTION

2.1. Chemicals and Reagents. The chemicals used in the present experiments were gold chloride hydrate, sodium borohydride (NaBH₄, 96%), citrate acid (AR, ≥99.5%), and (3-aminopropyl)trimethoxysilane (APTMS, 97%), which were purchased from Aladdin. The reagents and solvents, namely, hexadecyl trimethyl ammonium bromide (CTAB, AR), sodium

oleate (NaOL, CP), hydrochloric acid (HCl, AR, 37 wt % in water), L-ascorbic acid (AR), methanol (GR), and tetraethyl orthosilicate (TEOS, AR), were ordered from Sinopharm Chemical Reagent. Sodium hydroxide (NaOH, AR) and silver nitrate (AgNO₃) were bought from Macklin. Ultrapure water (18.2 MΩ cm⁻¹) was produced by a Millipore water purification system.

2.2. Synthesis of AuNRs. Following Ye et al.'s²⁶ method, AuNRs were prepared. Typically, 0.46 mL of fresh 0.01 M NaBH₄ solution was dissolved in 0.1 M CTAB in HAuCl₄ solution (10 mL, 0.5 mM) under rapid stirring until the color switched from yellow to light brown (about 2 h). The prepared compound solution was kept at RT for 30 min to use as a seed solution.

For AuNR growth, 1.82 g of 0.05 M CTAB and 0.304 g of 0.01 M NaOL in the end growth solution were dissolved in 50 mL of ultrapure water and gently stirred at 30 °C until a fair and fine solution was brought about, and then, 0.15 mL of 0.1 M AgNO₃ solution was added. After keeping the solution static for 15 min, 50 mL of 1 mM HAuCl₄ solution was added and continued to stir at 600 rpm prior to 90 min, unless the solution became colorless, and the pH value of 1.5 was regulated by adding 0.25 mL of HCl (37 wt %). Finally, 0.25 mL of 0.064 M AA and 0.04 mL of seed solution were added to the prepared growth solution and stirred at 1200 rpm. A sealed Erlenmeyer flask containing the prepared solution was kept in an oven at 30 °C for 12 h. The resulting AuNRs were finally collected by washing repeatedly by centrifugation and redispersed in 50 mL of water.

2.3. Synthesis of CDs. A simple one-step hydrothermal synthesis¹³ was used to prepare CDs by using citric acid as raw material. A mixture of 0.5 g of citric acid, 10 mL of APTMS, and 10 mL of ultrapure water was sonicated until the citric acid was completely dissolved, sealed in a stainless-steel autoclave with a PTFE liner, and kept in an oven at 180 °C for 12 h, and then, the mixture was cooled to ambient temperature. The mixture was centrifugally filtered and dialyzed with a dialysis membrane (molecular retention capacity of 100–500 Da) to remove excessive precursors and molecular impurities. The solution was finally rotary evaporated to obtain dry CDs.

2.4. Synthesis of AuNR@SiO₂. For the preparation of silica-coated AuNRs, 10 mL of the final synthesized AuNR solution was inserted in a 20 mL scintillation vial, to which 200 μL of 0.1 M NaOH base solution was used to adjust the pH level to 10–11. TEOS/methanol (30 μL, 20 wt %) was slowly injected into the above solution under gentle stirring, and after 48 h, the reaction was washed by centrifugation with water and ethanol simultaneously.

2.5. Synthesis of AuNR@SiO₂-CDs. Under magnetic stirring, 100 μL of CDs and 20 μL of 0.1 M NaOH base solution were added to 10 mL of AuNR@SiO₂ solution, and after 4 h of reaction at room temperature, 100 μL of CDs was added and stirred for another 4 h. Finally, AuNR@SiO₂-CDs were obtained by centrifugation and washed before usage.

2.6. Ice Recrystallization Inhibition (IRI) Experiment. A "splat cooling method"²⁷ was used to measure the IRI activity. For the experiments, an HCS621GXY hot and cold stage and a Zeiss Scope A1 microscope equipped with a CCD camera were employed. Specimens (10 μL) were dropped from a height of 1.5 m at ambient temperature onto a quartz glass sheet freshly removed from a -80 °C cryogenic refrigerator, thus forming a thin layer of solid ice. The quartz glass sheet was quickly placed in a cold table precooled to -20

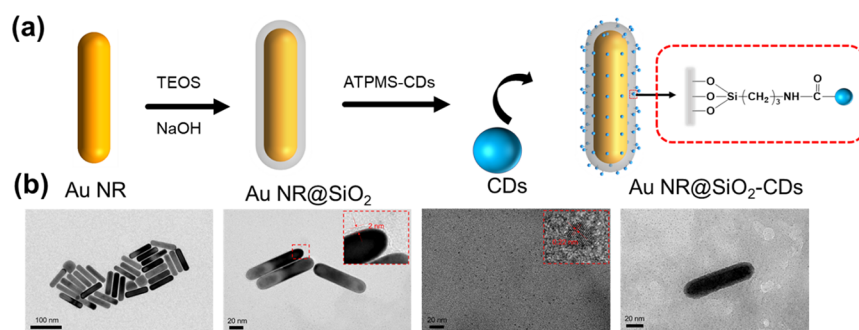


Figure 1. Preparation of the Au-CD nanomaterials (AuNR@SiO₂-CDs): (a) schematic illustration of the synthesis route and (b) TEM images of route stages.

°C, raised to -6 °C at a rate of 5 °C/min, and then annealed for 30 min. During this process, the ice crystal size was recorded with a CCD camera to obtain the size distribution of the ice crystals. The temperature and time variations were also recorded with accompanying temperature control software. ImageJ was used to measure the size of the ice crystals.

2.7. Modified Ice Affinity Experiments. Geng et al.'s¹⁰ experiment method was followed to modify the ice affinity; the sample with an initial concentration of 1.0 mg/mL was set as a standard. A liquid nitrogen device placed above the centrifuge tube was used as a cooling body, and the solution started to freeze from top to bottom. The ice was removed, and the melted solution was tested for concentration using a UV–vis spectrometer. This process was cycled about 20 times, and the experiment was repeated three times to take the average value.

2.8. In Vitro Cytotoxicity Assay. Hela cells were inoculated into 96-well plates at a density of 8000 cells per well. One control group and six experimental groups were set up for each concentration and incubated at 5% CO₂ and 37 °C for 24 h. Nanomaterials at different concentrations (1 , 2 , 5 , 10 , 20 , 50 , and 100 μg/mL) were then added to the 96-well plates. After 24 h, 10 μL of the MTT reagent was added to each well. Hela cells were then incubated for 4 h to form blue crystals, and 200 μL of DMSO was added to each well. After 10 min of shaking, the absorbance of the cells at 492 nm was measured with a microplate reader (EMax Plus), and the final data were obtained by subtracting the background.

2.9. Cell Cryopreservation and Recovery. A number of cells were centrifuged at 1500 rpm for 5 min, and 600 μL of DMEM medium was added to form a cell suspension and divided equally into six cell freezer tubes (six copies). PBS (100 μL) and glycerol, polyvinyl alcohol, hydroxyethyl starch, and gold nanorods@silica-carbon dots (two samples) dissolved in PBS solution were added to the cell freezing tubes where the final concentrations of glycerol, polyvinyl alcohol, hydroxyethyl starch, and AuNR@SiO₂-CDs dots were 35 mg/mL, 1 mg/mL, 35 mg/mL and 50 μg/mL, and 100 μg/mL, respectively. The cell freezing tubes were stored in a refrigerator at 4 °C for 10 min and then restored at -20 °C for 30 min. Finally, at -80 °C for 24 h, the tubes were rewarmed in a water bath, with an 808 nm laser.

3. RESULTS AND DISCUSSION

3.1. Synthesis of the Gold Nanorod and Carbon Dot Hybrid (AuNR-CD) Materials. In order to regulate the ice crystals' formation/growth and accelerate the rewarming process, highly uniformed and yielded AuNR@SiO₂-CD hybrid materials were designed subjected to the reported

procedures by Ye et al.²⁶ with slight targeted modification in the aspect ratio, which we have summarized in three synthetic stages. Figure 1a presents the schematic illustration, and panel b is the corresponding TEM image of the synthesis route of the hybrid material (AuNR@SiO₂-CDs).

In the first stage, AuNRs were synthesized by a seed-mediated method.²⁸ Employing a binary surfactant (CTAB/sodium oleate), AuNRs' slow reduction growth on Au seeds with ascorbic acid in CTAB/sodium oleate solution was followed by the rapid reduction of the precursors with sodium borohydride. In the second stage, the modified Stöber method²⁹ in an alkaline environment was applied to coat a mesoporous silica layer on the AuNRs. Finally, in the third stage, the AuNRs and CDs were linked to form AuNR@SiO₂-CDs via the condensation process. The complexity in synthesis is to obtain the desired aspect ratio of AuNRs and consolidation evidence of the AuNR and CDs. The peak position of isoplasmon resonance absorption (IPRA) on the local surface of the AuNR is closely associated to its aspect ratio. A little modification in the aspect ratio has significant consequences on the optical properties of AuNRs.^{30,31} In our work, AuNRs with different aspect ratios were prepared. The IPRA peak was analyzed by UV–visible-light absorption spectrum results, and the detailed description is shown in Figures S1–S3. Succinctly, ~ 4.4 is considered as the appropriate aspect ratio for higher photothermal conversion efficiency.

The AuNR@SiO₂-CD-associated synthesized components were examined by transmission electron microscopy (TEM, JEM-2100F) for morphological characterization. Figure 1b shows that the moderate size of AuNRs is uniform, and only a small number of spherical particles exist, but the final forming quality is good without the surfactant CTAB residue. The concentrated size is ~ 70 nm long and ~ 17 nm wide (thickness) having an aspect ratio of (length/width) ~ 4.4 . The carbon dots (CDs) are also uniformly dispersed; the lattice size spacing between the carbon points on the plane is 0.22 nm, indicating good crystallinity. The average particle size is ~ 3 nm, which is close to the critical size for ice nuclei. The detailed size distribution statistics of AuNRs and CDs is presented in Figure S4. The mesoporous SiO₂-coated monodisperse layer encapsulating AuNRs has a thickness of ~ 2 nm, to avoid the quenching effect and gold aggregation between CDs and AuNR@SiO₂ originating from hydrolysis of alkoxy methyl silyl groups of AuNRs. Carbon dots (CDs) reacted with AuNR@SiO₂ under alkaline conditions to form a stable covalent bond linkage with the silica shell layer and clustered on the surface of AuNRs. No large amount of

impurity agglomeration was observed, indicating the high monodispersity of the hybrid material AuNR@SiO₂-CDs.

To further validate the synthesis and composition of AuNR@SiO₂-CDs, the samples were analyzed by group characteristic peaks using a Fourier transform infrared spectrometer (iSSOR FT-IR) before and after the connection of CDs. The IR spectrograms are presented in Figure 2a. The

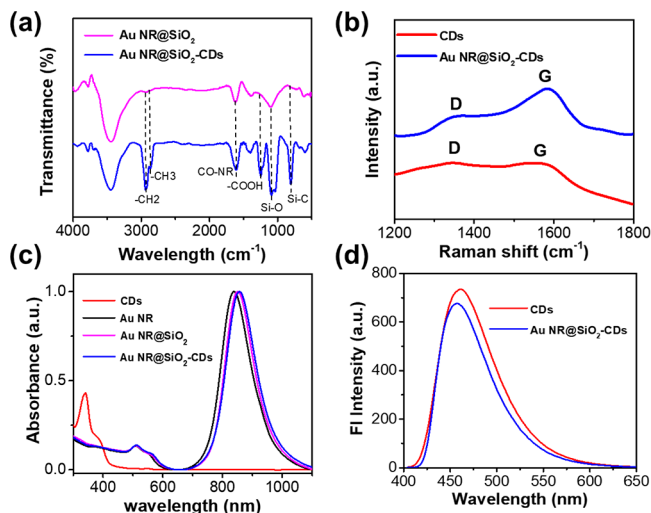


Figure 2. Characterization of synthesized AuNR@SiO₂-CDs and associated components. (a) FT-IR spectra, (b) Raman spectroscopy, (c) UV-visible absorption spectra, and (d) fluorescence spectra excited at 376 nm.

two characteristic peaks at 2925 and 2870 cm⁻¹ indicate the -CH₂ and -CH₃ ethylene/methylene groups, originating from salinized carbon dots. Peaks at 1250 and 1650 cm⁻¹ are ascribed to the linkage of CO-NR and -COOH, which is

evidence of the APTMS and CD linkage; the other peaks at 1080 and 800 cm⁻¹ are typical of the Si-O and Si-C bonds. The existence of a hydrophilic group (-COOH) and a hydrophobic group (-CH₃) provides support for regulating the formation and growth of ice. The results demonstrate the formation of stable bonding of the CDs and AuNR@SiO₂ via hydrolysis and condensation of APTMS on CDs, which is further endorsed by Raman spectroscopy in Figure 2b. The D peak at 1350 cm⁻¹ and the G peak at 1580 cm⁻¹ denote the defects and crystallinity of CDs, respectively, and the intensity ratio of the D peak to G peak (D/G) represents minor structural disorder and defect degree of the CDs.¹² There is some disordered arrangement in the periphery of the CD lattice, which provides structural support for the subsequent application of ice crystal control. Owing to the interference of fluorescence, only a broad Raman peak of the CDs appears, while the corresponding peak of the Raman spectrum of the AuNR@SiO₂-CDs is significantly enhanced. On the other hand, the near-field effect of the AuNRs has a certain quenching effect on fluorescence and weakens the interference of fluorescence on its Raman peak. The results are attributed to the enhancement of the Raman spectrum of CDs by AuNRs.

The optical and fluorescence properties of each synthesized component were characterized by UV-visible spectroscopy and fluorescence spectrometry, respectively, to ensure the design validation of the modified multimodal AuNR@SiO₂-CD hybrid material. The results are presented in Figure 2c. The CDs have a sharp narrow absorption peak at 350 nm with a narrow UV-light region, associated with the n-π* transition of the C=O bond, while AuNRs exhibit both the significant longitudinal peak and weak transverse absorption peaks at ~834 and ~520 nm, respectively. By considering the TEM images, the stronger longitudinal absorption peak is attributed to the high quality of the monodisperse colloidal AuNRs, and

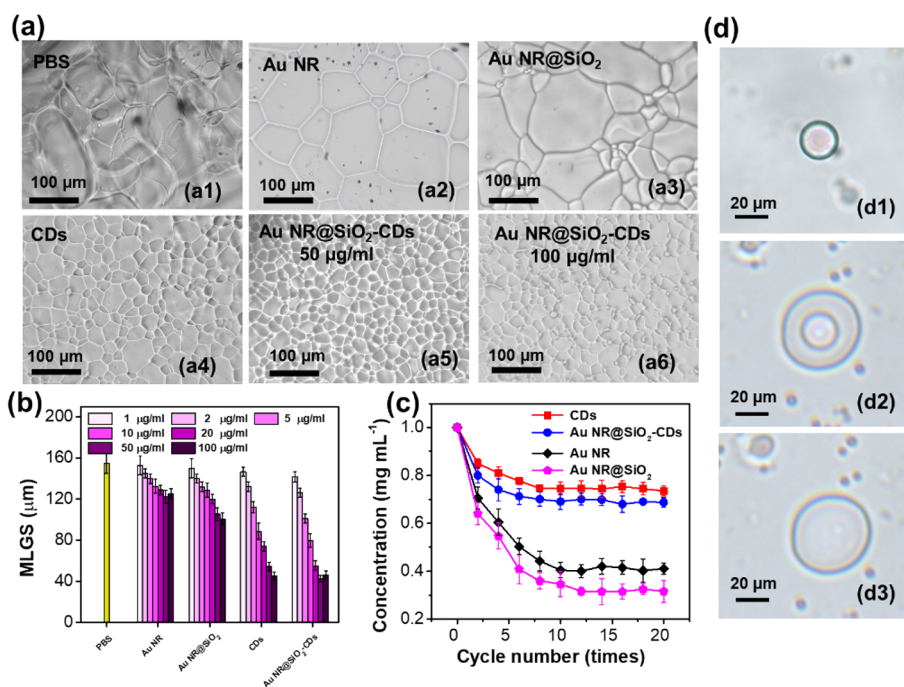


Figure 3. (a) Optical microscopic photographs of IRI: (a1) PBS solution, (a2) AuNR, (a3) AuNR@SiO₂, (a4) CDs, (a5) AuNR@SiO₂-CDs (50 µg/mL), and (a6) AuNR@SiO₂-CDs (100 µg/mL). (b) Quantitative analysis of IRI of AuNR@SiO₂-CDs and associated components in PBS solution. (c) Ice affinity test for different samples. (d) Process of recrystallization of single ice crystals: (d1) 0, (d2) 5, and (d3) 10 s.

the peak is redshifted to about ~ 20 nm for AuNR@SiO₂ and AuNR@SiO₂-CDs, which is the function of the increment in the local refractive index of the medium created by SiO₂ coating around the AuNRs. The connection of CDs has almost no effect on the peak-to-peak absorption of AuNR@SiO₂-CDs. Even though the peak-to-peak absorption of the hybrid material is redshifted, absorption still remains strong at 808 nm. Thus, the results inferred that the AuNR@SiO₂-CDs have excellent photothermal conversion efficiency at the laser induction of 808 nm. Figure S2 shows direct evidence. Photoluminescence is an inherent physical property of CDs. When the absorption peak of AuNRs is close to the fluorescence excitation wavelength of CDs, the fluorescence enhancement effect will occur; otherwise, fluorescence quenching will occur. The silica coating not only isolates CTAB inside but also avoids direct contact between AuNRs and CDs. The fluorescence emission of CDs and AuNR@SiO₂-CDs remained almost the same at ~ 450 nm under the fluorescence excitation of 376 nm having slight quenching due to the contiguity to the AuNRs, indicating that SiO₂ acts as the spacer and providing hindrance for complete quenching (Figure 2d).

All the above results indicate the successful synthesis of AuNR@SiO₂-CD hybrid materials.

3.1.1. Ice Recrystallization Inhibition (IRI) Activity. As reported by Wang et al.,¹² CDs may adsorb on the exterior of ice crystals and be able to inhibit the rapid growth of large ice crystals by engulfing small ice crystals during ice growth, and as a result, the morphology of ice crystals is modified. On the other hand, the change of shape size and growth during IRI will cause mechanical damage to the cell membrane during the rewarming process of cryopreservation.³² In order to verify cryopreservation application, the IRI ability is the most important index to evaluate biomimetic cryopreservative materials. The IRI ability was compared for each synthesized component and the ice crystal sizes of PBS solutions with different concentrations of AuNR@SiO₂-CD nanoparticles (see methods for details). The results were photographed under the microscope and are presented in Figure 3a. In the neat PBS solution, the ice crystal edges are smooth, round, and wide, there is no change in ice morphology, and the intergaps can easily be filled by unfrozen water channels, which cannot prevent the interaction of the water–ice crystals to expand and brings out the bigger crystal size. The crystal size is significantly suppressed in the AuNR@SiO₂-CDs and forms a geometrical shape of nanoflowers like a polygonal network. The crystals' morphology is packed, which may restrict each other to prevent nonfrozen water from binding on the curved surface. Apparently, the morphology depicts the reduction in ice crystal size. The maximum ice crystal grain size in the PBS solution of neat PBS, AuNRs, and AuNR@SiO₂ reaches ~ 150 μm (Figure 3a1–a3), and the maximum size of ice crystals recrystallized in the PBS solution of CDs and AuNR@SiO₂-CDs is approximately ≤ 50 μm (Figure 3a4–a6). The results indicate the excellence of CDs' IRI ability. The capstone arose having the same ability of the AuNR@SiO₂-CDs as that of CDs, which indicate that the linkage of CDs and AuNR@SiO₂ brings out the emerging IRI hybrid material (AuNR@SiO₂-CDs).

The IRI abilities of AuNR@SiO₂-CDs and associated synthesized components in PBS solution were precisely analyzed quantitatively and are depicted in Figure 3b. The average maximum largest grain size (MLGS) represents the

average size of the 10 largest ice crystals. The smaller the MLGS value is, the better will be the IRI ability. In addition, the MLGS value is the function of the concentration of the PBS solution as well. The MLGS value of each sample at a low concentration of <10 $\mu\text{g}/\text{mL}$ is not much different from that of neat PBS, which is ~ 150 μm . With the increase of concentration >10 $\mu\text{g}/\text{mL}$, the MLGS value of PBS solution of AuNRs and AuNR@SiO₂ decreases correspondingly but with a low magnitude. The minimum MLGS is ~ 100 μm , suggesting that the IRI effect of both of these two samples could be considered negligible. However, the MLGS value of PBS solution of CDs and AuNR@SiO₂-CDs decreases substantially at the concentration of >10 $\mu\text{g}/\text{mL}$. Exclusively at 100 $\mu\text{g}/\text{mL}$, it decreased to ~ 40 μm , indicating that the IRI ability of CDs ameliorated with the increase in concentration. Again, the IRI ability of AuNR@SiO₂-CDs is not different from that of CDs at the concentration of ≤ 100 $\mu\text{g}/\text{mL}$, but the MLGS value increases slightly at a concentration of 100 $\mu\text{g}/\text{mL}$. The possible reason is that the abundant ions in PBS induce the agglomeration between AuNR@SiO₂ and CDs due to which the dispersion in the PBS solution deteriorates. Also, quantitative analysis suggests that the IRI of AuNR@SiO₂-CDs is admirable at the concentration of 50 $\mu\text{g}/\text{mL}$, which can not only control the IRI during the rewarming process but also accelerate the temperature recovery rate and improve the survival rate of cells (Figure 6) by taking advantage of the prime photothermal possessive properties of AuNRs.

The IRI material controls the ice crystals either by adsorbing on the surface via functional groups, lattice matching, or changing the surface state. The system reaches thermodynamically to the water molecule adsorption–escape equilibrium state to restrict the growth of ice crystals. Owing to having enriched functional groups, CDs inhibit ice formation via adsorbing on the surface of the ice. The ice affinity tests of AuNR@SiO₂-CDs and associated synthesized components were performed and are shown in Figure 3c. The concentration of CDs and AuNR@SiO₂-CDs decreases in the first few cycles and then tends to be flat, indicating that the adsorption of CDs to ice crystals is at an excited state at <10 cycles and reached an equilibrium state, at the concentration of ~ 0.75 mg/mL (75%). AuNR@SiO₂-CDs exhibit a similar trend at a final concentration of ~ 0.70 mg/mL (70%), whereas AuNRs and AuNR@SiO₂ reveal their poor adsorption equilibrium state at ~ 40 and $\sim 32\%$, respectively. The initial decrease during the earlier cycles is apparently due to the decrease in the number of the CDs entrapped between the ice polygonal crystals because of the growth rate in action (supercooling law). At the later cycles, the adsorption equilibrium state is generated, and enough quantity of the CDs reaches the ice melt.

IRI is a process in which ice crystals are reformed and grow rapidly at the expense of small ice crystals during the temperature change. A small amount of PBS droplets was added to a crucible filled with silicone oil, and the overall temperature was controlled to form ice nuclei. Then, under certain temperature control, the recrystallization process of individual ice crystals from small to large was observed. Figure 3d implies the ice shaping and growth behavior of the single ice crystals during the recrystallization process. The initial size of a single ice crystal is about 20 μm , and it appears as a smooth disk shape. When the overall temperature is changed from -2 °C at a heating rate of 1 °C/min, the large ice crystals swallow the surrounding smaller ice crystals and form large ice crystal nuclei. In the end, the ice crystals were completely

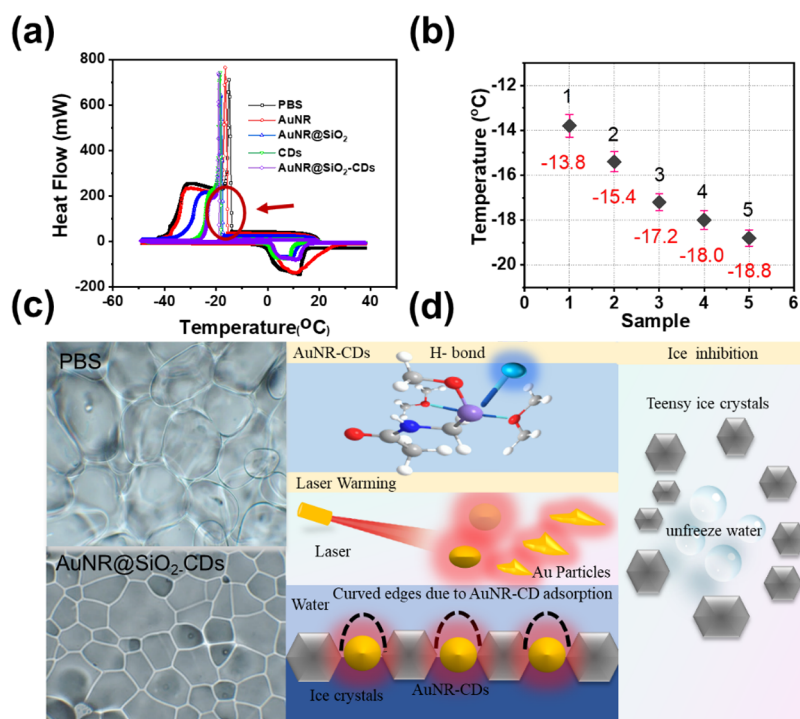


Figure 4. (a) DSC thermographs of AuNR@SiO₂-CDs and associated synthesized components. (b) Transition temperature values of 1; PBS, 2; AuNR, 3; AuNR@SiO₂, 4; CDs, 5; AuNR@SiO-CDs extracted from DCS graphs. (c) Ice crystal morphology comparison with PBS solution. (d) Schematic of the possible adsorption inhibition mechanism of AuNR@SiO-CDs.

swallowed, and the size of the regrown ice crystals became larger to $\sim 40 \mu\text{m}$ and changed into an abrupt hexagonal shape. The aforementioned shape of the ice is much supportive to allow the IRI material to merge among the ice hexagonal edges.

Ice-resistant materials can effectively regulate the freezing temperature of water through the adsorption–inhibition mechanism. According to the Kelvin effect,¹¹ AFMs selectively adsorbed on the surface of ice crystals to produce planar bending, thus inhibiting growth. We expect that AuNR@SiO₂-CDs exhibit a similar effect by imitating their structural principle. The biomimetic antifreezing properties of the materials were studied by carrying out a DSC test to verify the regulated ice freezing temperature as shown in Figure 4a. For this purpose, AuNR@SiO₂-CDs and associated synthesized components were dissolved in phosphate-buffered saline (PBS), and the final concentration of the test was selected as 100 $\mu\text{g}/\text{mL}$. At a constant cooling rate of 10 $^{\circ}\text{C}/\text{min}$, a large amount of heat was released at the temperature of neat PBS solution. The temperatures are drawn in Figure 4b. The PBS solution has a releasing temperature of $-13.8 \text{ }^{\circ}\text{C}$; similarly, AuNRs, AuNR@SiO₂, CDs, and AuNR@SiO-CDs released heat at -15.4 , -17.2 , -18 , and $-18.8 \text{ }^{\circ}\text{C}$, respectively. It shows that AuNR@SiO₂-CDs can effectively reduce freezing temperatures. Comparing neat PBS solution, the freezing temperature of AuNR@SiO₂-CDs is reduced by almost 5 $^{\circ}\text{C}$.

Considering all the above ice recrystallization results indicate the perspectives that the linkage of CDs increases the affinity of the entire hybrid material (AuNR@SiO-CDs) to ice crystals and the other is that AuNRs and AuNR@SiO₂ can only control the formation and growth of ice crystals through an adsorption–inhibition mechanism. The reason for the ice inhibition mechanism can be hypothesized by the following two points. (i) At the molecular level, carboxylic ($-\text{COOH}$) and epoxy ($-\text{O}-$) groups from CDs are likely to form a

hydrogen bond with the ice (H_2O) because of differences in valency or electronegativity. The oxygen O atom and hydroxyl OH serve as binding sites and authorize the AuNR@SiO₂-CDs with the ability to govern the ice affinity. The interaction of CDs–ice generates a more nonfreezing water fraction. This is evidenced by the lowering in the ice crystal freezing temperature in Figure 4b, and the schematic is shown in Figure 4d. (ii) Considering Figure 4a–c, it is expected that the Kelvin effect is developed, and the hybrid material (AuNR@SiO-CDs) is adsorbed on the surface of the ice and creates the microcurvatures; the sharp edges appeared due to incorporations of CDs (from the hybrid material) among the ice crystals. This could be demonstrated by the size reduction of the crystals (Figure 4c); it was previously reported^{11,33} that AFPs can bind with the prism surfaces of the ice crystals and constitute small layers of ice, which restrict the growth. We proposed that the decrease in the MLGS value of AuNR@SiO-CDs (Figure 3b) indicates the existence of more convex surfaces of ice and thus the flexure of the new ice crystals, which may hinder the further growth of the crystals. The proposed schematic illustration is given in Figure 4c.

3.2. Photothermal Properties. Rapid thawing without cell damage is a matter of contention of anti-icing materials; photothermal conversion by laser irradiation is the best tool to overcome the concerns that occur during the recrystallization of ice. The heat generated by an 808 nm laser with a power density of 1 W/cm^2 has a small increase in the temperature of the auxiliary rewarming, and increasing the laser power density improves the rewarming effect. The intense resonance of the surface plasmon of AuNRs under high-power laser irradiation can promote the transformation shape of AuNRs to spherical.³⁴ In order to maintain the structural stability of AuNR@SiO₂-CDs, 2 W/cm^2 of an 808 nm laser was used to achieve a faster auxiliary rewarming effect.

In the case of no water bath at room temperature, AuNR@SiO₂-CD PBS solutions with different concentrations were exposed to 2 W/cm² laser irradiation for 2 min, and their photothermal images were recorded by an IR camera, as shown in Figure 5a. The samples at the prepared concentrations of 1,

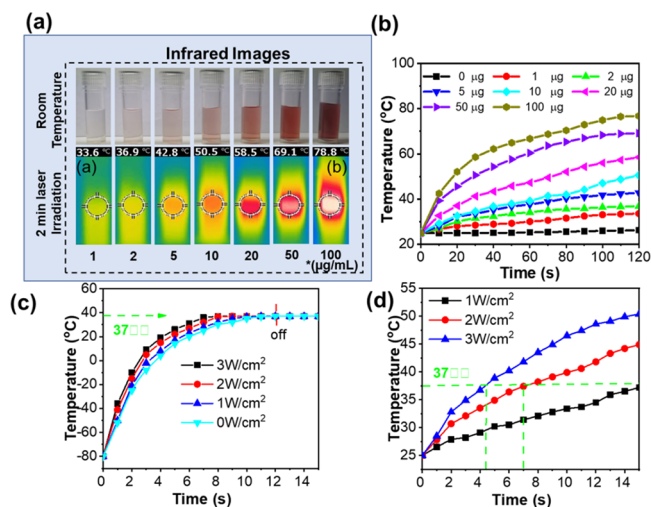


Figure 5. (a) Photothermal images of AuNR@SiO₂-CDs. (b) Photothermal curves of AuNR@SiO₂-CDs. Photothermal curves of AuNR@SiO₂-CDs under different power laser irradiation: (c) water bath with a laser. (d) Laser irradiation at room temperature.

2, 5, 10, 20, 50, and 100 µg/mL in PBS solution could reach the temperatures of 33.6, 36.9, 42.8, 50.5, 58.5, 69.1, and 78.8 °C, respectively. The IR images signify that the central area of temperature radiation is located in the middle of the solution in the centrifuge tube, indicating that the AuNR@SiO₂-CDs have excellent dispersibility and there are no agglomeration precipitates at the bottom.

At the same time, the absorption of laser light by the AuNRs that penetrated in the solution is converted into heat energy to radiate the entire cell cryopreservation tube and result in rising temperature. The recorded temperature within 2 min is plotted in Figure 5b. All of the samples show elevation in temperature and reached a plateau at 2 min. Furthermore, at the constant power density and concentration of >5 µg/mL, the temperature of all samples exceeds 37 °C (i.e., at this temperature, mechanical damage to cells can be avoided). In order to gain an in-depth understanding, samples were investigated at various laser power densities. The temperature rise observation at the representative concentration of 50 µg/mL and at a constant temperature of 37 °C (the mentioned temperature can avoid mechanical damage of cells) by a laser-assisted environment and without laser supply after 37 °C is shown in Figure 5c. The rate of temperature is proportional to the laser power density. Interestingly, while increasing the laser power density to 2 or 3 W/cm², the time required for samples to reach 37 °C becomes longer to about 2 s in the absence of a laser-irradiated dose. Similarly, sample temperature rising behavior was also observed at room temperature (see Figure 5d). With a laser power density of 1 W/cm², the temperature of the AuNR@SiO₂-CD PBS solution was regulated from 25 to 37 °C in 15 s, while under the laser irradiation of 2 or 3 W/cm², the temperature reached 37 °C before reaching the time of 8 s. Based on the above observations, the 808 nm laser power density of 2 W/cm² is considered to be an optimal

choice to irradiate and disperse well the AuNR@SiO₂-CDs in PBS solution, which not only provides full display of the laser-induced heating effect but also keeps the shape of the AuNR from diversity.

3.3. Cytotoxicity Assay. The MTT assay is used to detect the toxicity of synergistic efficacy of CDs, AuNR@SiO₂, and AuNR@SiO₂-CDs to Hela cells. Taking the neat PBS solution as the control group whose cell viability was set at 100% and the other three samples as the experimental group, Figure 6a

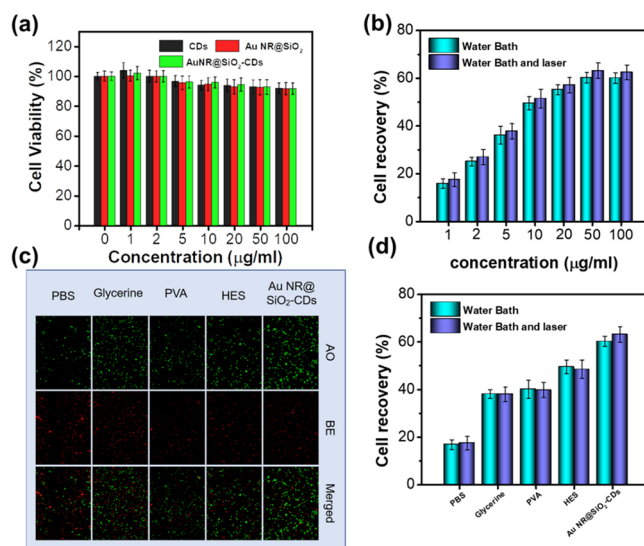


Figure 6. (a) MTT assay for measuring cytotoxicity. (b) Cell recovery at various concentrations of AuNR@SiO₂-CDs. (c) Fluorescence micrographs of alive (green) and dead (red) cells under different cryoprotectants. (d) Cell recovery under different cryoprotectants.

shows the cell viability at the concentration range of 0–100 µg/mL. All of the samples in experimental groups show only a slight decrease in the cell viability with the increase in concentration, but interestingly, the survival rate of all samples is sustained to >90%. Within the allowable range of cell inactivation, the experimental group is considered to have low cytotoxicity and good biocompatibility to cells. Furthermore, for cryopreservation and rewarming, the cells were frozen and rewarmed. The survival rate of Hela cells was detected by double staining of the mortality rate of alive and dead cells. Figure 6b shows the survival rate data of cells under the protection of different concentrations of AuNR@SiO₂-CDs after cryopreservation and rewarming in the presence of a water bath and laser assistance dose. In both of the surroundings, the gradual increase in cell recovery is observed up to ~60% at 100 µg/mL. Likewise, the cell recovery in a laser-assisted (2 W/cm²) environment significantly improved to 3–4% compared to that in the pure water bath.

The performance of the AuNR@SiO₂-CDs with the other commonly used cryoprotectants such as glycerol, polyvinyl alcohol, and hydroxyethyl starch was also examined. Figure 6c shows the fluorescence image of cells under a fluorescence microscope: the green display represents alive cells with intact cell membranes, and the red display represents dead cells with damaged cell membranes. The results depict that the AuNR@SiO₂-CDs have a high and dense green fluorescence area and there is a negligible dead cell portion, indicating that the cryoprotective effect is comparatively superior to that of other common cryoprotectants.

Figure 6d shows comparison data of the cell survival rate after cryopreservation and rewarming for the different cryoprotectants and AuNR@SiO₂-CDs. The cell survival rates in common cell cryoprotectants such as PBS, glycerol, polyvinyl alcohol, and hydroxyethyl starch are 18, 38, 40, and 49%, respectively, in which PBS solution shows the lowest 18% and AuNR@SiO₂-CDs is the highest with 60%. Moreover, in the laser-irradiated environment, there is no obvious change effect except for the AuNR@SiO₂-CDs. The results clearly confirm that the AuNR@SiO₂-CD hybrid materials have efficient performance for the cryopreservation of HeLa cells.

4. CONCLUSIONS

In this paper, utilizing the ice recrystallization inhibition ability of bionic ice control materials (CDs) and the excellent photothermal conversion ability of nanomaterials (AuNRs), nanohybrid materials (AuNR@SiO₂-CDs) with both properties were synergistically designed by the improved Stöber method. The optimal photothermal conversion efficiency is regulated by controlling the surface functional groups and size structure. It was determined that the photothermal conversion efficiency reaches the highest value at the optimal aspect ratio of gold nanorods of ~ 4.4 and the local surface isoelectrification ion absorption peak of AuNR@SiO₂-CDs near 808 nm. Furthermore, at the concentration of 50 $\mu\text{g}/\text{mL}$, AuNR@SiO₂-CDs exhibit outstanding IRI ability. The abundant functional groups of CDs provide excellent ice affinity for hybrid materials. Under the irradiation of 808 nm, an excitation power of 2 W/cm², and a concentration 50 $\mu\text{g}/\text{mL}$, AuNR@SiO₂-CDs can reach 37 °C in 8 s, which meets the requirements of cell reheating temperature. The material performances were also applied to the cryopreservation and rewarming of HeLa cells. The cytotoxicity test showed that the cell survival rate of the hybrid material was >90% even at high concentrations (1000 $\mu\text{g}/\text{mL}$), with no cytotoxicity. In the absence of other organic compounds, the survival rate of HeLa cells was >60%, which is further improved up to 4% after laser-assisted rewarming. We expect that the synthesized material has an excellent performance in the field of cryopreservation and cell rewarming.

■ ASSOCIATED CONTENT

SI Supporting Information

The Supporting Information is available free of charge at <https://pubs.acs.org/doi/10.1021/acsomega.3c00079>.

Information on the laser irradiation dose and gold nanorod size selection: (Figure S1) TEM images and corresponding absorption curves of AuNRs with different aspect ratios; (Figure S2) temperature variation of AuNRs with different aspect ratios under laser irradiation of corresponding wavelengths; (Figure S3) TEM images of AuNRs wrapped in silicon with different aspect ratios; (Figure S4) size statistics of AuNRs and CDs (PDF)

■ AUTHOR INFORMATION

Corresponding Authors

Sarmad Ali – *Institute of Solid-State Physics, Chinese Academy of Sciences, Hefei, Anhui 230031, China; Key Laboratory of Photovoltaic and Energy Conservation Materials, Hefei Institutes of Physical Science, Chinese Academy of Sciences,*

Hefei, Anhui 230031, China; orcid.org/0000-0002-1424-3367; Email: ali@issp.ac.cn

Min Xi – *Institute of Solid-State Physics, Chinese Academy of Sciences, Hefei, Anhui 230031, China; Key Laboratory of Photovoltaic and Energy Conservation Materials, Hefei Institutes of Physical Science, Chinese Academy of Sciences, Hefei, Anhui 230031, China; orcid.org/0000-0003-4414-3110; Email: minxi@issp.ac.cn*

Nian Li – *Institute of Solid-State Physics, Chinese Academy of Sciences, Hefei, Anhui 230031, China; Key Laboratory of Photovoltaic and Energy Conservation Materials, Hefei Institutes of Physical Science, Chinese Academy of Sciences, Hefei, Anhui 230031, China; Email: linian@issp.ac.cn*

Authors

Shenyi Ding – *Institute of Solid-State Physics, Chinese Academy of Sciences, Hefei, Anhui 230031, China; Key Laboratory of Photovoltaic and Energy Conservation Materials, Hefei Institutes of Physical Science, Chinese Academy of Sciences, Hefei, Anhui 230031, China; orcid.org/0000-0002-6967-9790*

Shudong Zhang – *Institute of Solid-State Physics, Chinese Academy of Sciences, Hefei, Anhui 230031, China; Key Laboratory of Photovoltaic and Energy Conservation Materials, Hefei Institutes of Physical Science, Chinese Academy of Sciences, Hefei, Anhui 230031, China; orcid.org/0000-0002-0215-1641*

Jun Zhao – *Institute of Solid-State Physics, Chinese Academy of Sciences, Hefei, Anhui 230031, China; Key Laboratory of Photovoltaic and Energy Conservation Materials, Hefei Institutes of Physical Science, Chinese Academy of Sciences, Hefei, Anhui 230031, China; orcid.org/0000-0002-1410-6039*

Cui Liu – *Institute of Solid-State Physics, Chinese Academy of Sciences, Hefei, Anhui 230031, China; Key Laboratory of Photovoltaic and Energy Conservation Materials, Hefei Institutes of Physical Science, Chinese Academy of Sciences, Hefei, Anhui 230031, China*

Muhammad Adnan Aslam – *Institute of Solid-State Physics, Chinese Academy of Sciences, Hefei, Anhui 230031, China; Key Laboratory of Photovoltaic and Energy Conservation Materials, Hefei Institutes of Physical Science, Chinese Academy of Sciences, Hefei, Anhui 230031, China*

Xinling Yu – *Institute of Solid-State Physics, Chinese Academy of Sciences, Hefei, Anhui 230031, China; Key Laboratory of Photovoltaic and Energy Conservation Materials, Hefei Institutes of Physical Science, Chinese Academy of Sciences, Hefei, Anhui 230031, China*

Lei Pan – *Institute of Solid-State Physics, Chinese Academy of Sciences, Hefei, Anhui 230031, China; Key Laboratory of Photovoltaic and Energy Conservation Materials, Hefei Institutes of Physical Science, Chinese Academy of Sciences, Hefei, Anhui 230031, China*

Zhenyang Wang – *Institute of Solid-State Physics, Chinese Academy of Sciences, Hefei, Anhui 230031, China; Key Laboratory of Photovoltaic and Energy Conservation Materials, Hefei Institutes of Physical Science, Chinese Academy of Sciences, Hefei, Anhui 230031, China; orcid.org/0000-0002-0194-3786*

Complete contact information is available at: <https://pubs.acs.org/doi/10.1021/acsomega.3c00079>

Author Contributions

N.L., M.X., and Z.W. designed and engineered the samples; S.D., S.A., and M.X. performed the experiments; S.D. and S.A. have analyzed the data and wrote the paper with support. The paper was discussed and revised by S.Z., J.Z., C.L., X.Y., M.A.A., M.X., L.P., N.L., Z.W., and S.A. All authors contributed to the general discussion.

Notes

The authors declare no competing financial interest.

ACKNOWLEDGMENTS

This work was financially supported by the National Key Research and Development Project (2020YFA0210703), the National Natural Science Foundation of China (nos. U2032159, U2032158, 62005292, 52171053, and 12204488), the Major Scientific and Technological Special Project of Anhui Province (202103a05020013), the Key Research and Development Program of Anhui Province (202104a05020036), the Collaborative Innovation Program of Hefei Science Center, CAS (2020HSC-CIP003), the Major Scientific and the CASHIPS Director's Fund (YZJJZX202018 and YZJJZX202015), the Natural Science Foundation of Anhui Province (2208085ME109 and 2208085QE132), and the Special Fund Project for Local Science and Technology Development Guided by the Central Government of Anhui Province (202107d08050016).

REFERENCES

- (1) Joukhdar, H.; Seifert, A.; Jüngst, T.; Groll, J.; Lord, M. S.; Rnjak-Kovacina, J. Ice templating soft matter: fundamental principles and fabrication approaches to tailor pore structure and morphology and their biomedical applications. *Adv. Mater.* **2021**, *33*, No. 2100091.
- (2) Zhao, Z.; Chen, H.; Liu, X.; Liu, H.; Zhang, D. Development of high-efficient synthetic electric heating coating for anti-icing/de-icing. *Surf. Coat. Technol.* **2018**, *349*, 340–346.
- (3) Zhu, Z.; Zhou, Q.; Sun, D.-W. Measuring and controlling ice crystallization in frozen foods: A review of recent developments. *Trends Food Sci. Technol.* **2019**, *90*, 13–25.
- (4) Nilssen, K.; Klein-Paste, A.; Wählin, J. The effect of additives on the low temperature ice-melting capacity of NaCl. *Transportation research record* **2018**, *2672*, 158–166.
- (5) Yan, Y.; Luo, N.; Xiang, X.; Xu, Y.; Zhang, Q.; Zhan, X. Fabricating mechanism and preparation of anti-icing & icephobic coating. *Prog. Chem.* **2014**, *26*, 214.
- (6) He, Z.; Liu, K.; Wang, J. Bioinspired materials for controlling ice nucleation, growth, and recrystallization. *Acc. Chem. Res.* **2018**, *51*, 1082–1091.
- (7) Chang, T.; Zhao, G. Ice inhibition for cryopreservation: materials, strategies, and challenges. *Adv. Sci.* **2021**, *8*, 2002425.
- (8) He, Z.; Wu, C.; Hua, M.; Wu, S.; Wu, D.; Zhu, X.; Wang, J.; He, X. Bioinspired multifunctional anti-icing hydrogel. *Matter* **2020**, *2*, 723–734.
- (9) Liu, M.; Zhang, X.; Guo, H.; Zhu, Y.; Wen, C.; Sui, X.; Yang, J.; Zhang, L. Dimethyl sulfoxide-free cryopreservation of chondrocytes based on zwitterionic molecule and polymers. *Biomacromolecules* **2019**, *20*, 3980–3988.
- (10) Geng, H.; Liu, X.; Shi, G.; Bai, G.; Ma, J.; Chen, J.; Wu, Z.; Song, Y.; Fang, H.; Wang, J. Graphene oxide restricts growth and recrystallization of ice crystals. *Am. Ethnol.* **2017**, *129*, 1017–1021.
- (11) Bai, G.; Song, Z.; Geng, H.; Gao, D.; Liu, K.; Wu, S.; Rao, W.; Guo, L.; Wang, J. Oxidized quasi-carbon nitride quantum dots inhibit ice growth. *Adv. Mater.* **2017**, *29*, No. 1606843.
- (12) Wang, Z.; Yang, B.; Chen, Z.; Liu, D.; Jing, L.; Gao, C.; Li, J.; He, Z.; Wang, J. Bioinspired cryoprotectants of glucose-based carbon dots. *ACS Appl. Bio Mater.* **2020**, *3*, 3785–3791.
- (13) Abbas, A.; Mariana, L. T.; Phan, A. N. Biomass-waste derived graphene quantum dots and their applications. *Carbon* **2018**, *140*, 77–99.
- (14) Zhang, B.; Jiang, Y.; Balasubramanian, R. Synthesis, formation mechanisms and applications of biomass-derived carbonaceous materials: a critical review. *J. Mater. Chem. A* **2021**, 24759.
- (15) Yanhong, L.; Dongxu, Z.; Baodong, M.; Hui, H.; Yang, L.; Huaqiao, T.; Zhenhui, K. Progress in Carbon Dots from the Perspective of Quantum Dots [J]. *Acta Chim. Sin.* **2020**, *78*, 1349–1365.
- (16) Parvin, N.; Mandal, T. K.; Roy, P. Polyelectrolyte carbon quantum-dots: new player as a noninvasive imaging probe in *Drosophila*. *J. Nanosci. Nanotechnol.* **2013**, *13*, 6499–6505.
- (17) Manuchehrabadi, N.; Gao, Z.; Zhang, J.; Ring, H. L.; Shao, Q.; Liu, F.; McDermott, M.; Fok, A.; Rabin, Y.; Brockbank, K. G.; Garwood, M.; Haynes, C. L.; Bischof, J. C. Improved tissue cryopreservation using inductive heating of magnetic nanoparticles. *Sci. Transl. Med.* **2017**, *9*, No. eaah4586.
- (18) Panhwar, F.; Chen, Z.; Hossain, S. C.; Wang, M.; Haider, Z.; Memon, K.; Chen, P.; Zhao, G. Near-infrared laser mediated modulation of ice crystallization by two-dimensional nanosheets enables high-survival recovery of biological cells from cryogenic temperatures. *Nanoscale* **2018**, *10*, 11760–11774.
- (19) Khosla, K.; Wang, Y.; Hagedorn, M.; Qin, Z.; Bischof, J. Gold nanorod induced warming of embryos from the cryogenic state enhances viability. *ACS Nano* **2017**, *11*, 7869–7878.
- (20) Ketterer, B. Protective role of glutathione and glutathione transferases in mutagenesis and carcinogenesis. *Mutation Research/Fundamental and molecular mechanisms of mutagenesis* **1988**, *202*, 343–361.
- (21) Knothe, G. Dependence of biodiesel fuel properties on the structure of fatty acid alkyl esters. *Fuel Process. Technol.* **2005**, *86*, 1059–1070.
- (22) Zhang, J.; Zhao, Y.; Guo, X.; Chen, C.; Dong, C. L.; Liu, R. S.; Han, C. P.; Li, Y.; Gogotsi, Y.; Wang, G. ACS Appl. Mater. Interfaces. *Nat. Cata.* **2018**, *1*, 985–992.
- (23) Lu, W.; Wang, H.; Zhang, J.; Jiang, L. Gold nanorods: synthesis, growth mechanism and purification. *Prog. Chem.* **2015**, *27*, 785.
- (24) Lohse, S. E.; Murphy, C. J. The quest for shape control: a history of gold nanorod synthesis. *Chem. Mater.* **2013**, *25*, 1250–1261.
- (25) Murphy, C. J.; Thompson, L. B.; Chernak, D. J.; Yang, J. A.; Sivapalan, S. T.; Boulos, S. P.; Huang, J.; Alkilany, A. M.; Sisco, P. N. Gold nanorod crystal growth: From seed-mediated synthesis to nanoscale sculpting. *Curr. Opin. Colloid Interface Sci.* **2011**, *16*, 128–134.
- (26) Ye, X.; Zheng, C.; Chen, J.; Gao, Y.; Murray, C. B. Using binary surfactant mixtures to simultaneously improve the dimensional tunability and monodispersity in the seeded growth of gold nanorods. *Nano Lett.* **2013**, *13*, 765–771.
- (27) Tam, R. Y.; Rowley, C. N.; Petrov, I.; Zhang, T.; Afagh, N. A.; Woo, T. K.; Ben, R. N. Solution conformation of C-linked antifreeze glycoprotein analogues and modulation of ice recrystallization. *J. Am. Chem. Soc.* **2009**, *131*, 15745–15753.
- (28) Nikoobakht, B.; El-Sayed, M. A. Preparation and growth mechanism of gold nanorods (NRs) using seed-mediated growth method. *Chem. Mater.* **2003**, *15*, 1957–1962.
- (29) Wu, W.-C.; Tracy, J. B. Large-scale silica overcoating of gold nanorods with tunable shell thicknesses. *Chem. Mater.* **2015**, *27*, 2888–2894.
- (30) Scarabelli, L.; Sánchez-Iglesias, A.; Pérez-Juste, J.; Liz-Marzán, L. M. A “tips and tricks” practical guide to the synthesis of gold nanorods. *ACS Publications* **2015**, *6*, 4270–4279.
- (31) Chou, C.-H.; Chen, C.-D.; Wang, C. R. C. Highly efficient, wavelength-tunable, gold nanoparticle based optothermal nanoconvertors. *J. Phys. Chem. B* **2005**, *109*, 11135–11138.
- (32) Liu, K.; Wang, C.; Ma, J.; Shi, G.; Yao, X.; Fang, H.; Song, Y.; Wang, J. Janus effect of antifreeze proteins on ice nucleation.

Proceedings of the National Academy of Sciences **2016**, *113*, 14739–14744.

(33) Jin, S.; Yin, L.; Kong, B.; Wu, S.; He, Z.; Xue, H.; Liu, Z.; Cheng, Q.; Zhou, X.; Wang, J. Spreading fully at the ice-water interface is required for high ice recrystallization inhibition activity. *Science China Chemistry* **2019**, *62*, 909–915.

(34) Bai, G.; Gao, D.; Liu, Z.; Zhou, X.; Wang, J. Probing the critical nucleus size for ice formation with graphene oxide nanosheets. *Nature* **2019**, *576*, 437–441.